

Original

Schultze, L.K.P.; Merckelbach, L.M.; Carpenter, J.R.:
Turbulence and Mixing in a Shallow Shelf Sea From Underwater Gliders.
In: Journal of Geophysical Research : Oceans. Vol. 122 (2017) 11, 9092 - 9109.
First published online by AGU: 06.10.2017

<https://dx.doi.org/10.1002/2017JC012872>

RESEARCH ARTICLE

10.1002/2017JC012872

Turbulence and Mixing in a Shallow Shelf Sea From Underwater Gliders

Larissa K. P. Schultze¹ , Lucas M. Merckelbach¹, and Jeffrey R. Carpenter¹¹Helmholtz-Zentrum Geesthacht, Institute of Coastal Research, Geesthacht, Germany

Key Points:

- Two extensive continuous data sets spanning 29 days use gliders to quantify turbulence in a shallow (40 m) energetic shelf sea
- Turbulent fluxes within stratification are sensitive to the thermocline definition, mixing efficiency, and intermittent turbulent events
- A tendency for low bulk Richardson numbers to exhibit higher turbulence levels was observed; however, no clear relation could be drawn.

Supporting Information:

- Supporting Information S1
- Data Set S1
- Data Set S2
- Data Set S3
- Data Set S4

Correspondence to:

L. K. P. Schultze,
larissa.schultze@hzg.de

Citation:

Schultze, L. K. P., Merckelbach, L. M., & Carpenter, J. R. (2017). Turbulence and mixing in a shallow shelf sea from underwater gliders. *Journal of Geophysical Research: Oceans*, 122, 9092–9109. <https://doi.org/10.1002/2017JC012872>

Received 8 MAR 2017

Accepted 1 OCT 2017

Accepted article online 6 OCT 2017

Published online 23 NOV 2017

Abstract The seasonal thermocline in shallow shelf seas acts as a natural barrier for boundary-generated turbulence, damping scalar transport to the upper regions of the water column and controlling primary production to a certain extent. To better understand turbulence and mixing conditions within the thermocline, two unique 12 and 17 day data sets with continuous measurements of the dissipation rate of turbulent kinetic energy (ϵ) collected by autonomous underwater gliders under stratified to well-mixed conditions are presented. A highly intermittent ϵ signal was observed in the stratified thermocline region, which was mainly characterized by quiescent flow (turbulent activity index below 7). The rate of diapycnal mixing remained relatively constant for the majority of the time with peaks of higher fluxes that were responsible for much of the increase in bottom mixed layer temperature. The water column stayed predominantly strongly stratified, with a bulk Richardson number across the thermocline well above 2. A positive relationship between the intensity of turbulence, shear, and stratification was found. The trend between turbulence levels and the bulk Richardson number was relatively weak but suggests that ϵ increases as the bulk Richardson number approaches 1. The results also highlight the interpretation difficulties in both quantifying turbulent thermocline fluxes as well as the responsible mechanisms.

1. Introduction

Stratification in shelf seas occurs when wind stress and bottom friction do not compete sufficiently against solar heating at the ocean surface to mix the water column (Pingree & Griffiths, 1978; Simpson et al., 1990). Except for blooms, enhanced phytoplankton growth in stratified continental shelf seas concentrates in the subsurface chlorophyll maximum (SCM), which is usually situated in the euphotic, temperature stratified region of the water column. In this region, the thermocline, conditions for phytoplankton growth are often favorable due to the existing vertical gradients of light intensity, nutrients, O_2 , and CO_2 (Ross & Sharples, 2007; Simpson & Sharples, 2012). On a global scale, such rates of primary productivity in the SCM are thought to contribute significantly to both the fixation of carbon (Holligan et al., 1984; Richardson et al., 1998; Ross & Sharples, 2007) and biological production (Muller-Karger et al., 2005; Simpson & Sharples, 2012). Understanding the mechanisms through which different scalars are transported to and across the stratified thermocline are therefore of major importance.

In several areas of the German Bight of the North Sea (Figure 1), the water column stratifies during the summer months and a thermocline separates the surface and bottom layers, which remain well mixed to a large extent (van Leeuwen et al., 2015). The upward nutrient and downward heat transport across the thermocline in shelf seas are thought to be dominated by low energy mechanisms other than directly by the highly energetic barotropic tide (Palmer et al., 2008; Rippeth, 2005; van Haren et al., 1999). van Haren et al. (1999) suggested that the dissipation of breaking internal waves in combination with near-inertial current shear is responsible for mixing and nutrient transport across the thermocline. Rippeth (2005) studied mixing in an area of relative smooth topography and identified the breaking of internal tides and near-inertial oscillations as key processes to understand mixing in the thermocline. Palmer et al. (2008) analyzed a 50 h data set of microstructure shear measurements using a vertical free-falling profiler. They suggested that turbulence and mixing across the thermocline in the Celtic Sea are powered by internal waves and near-inertial waves. The most accepted idea on how the energy generated by possible mixing processes is delivered to the thermocline is the transition to turbulent flow through shear instability (Burchard & Rippeth, 2009; Palmer et al., 2008; Rippeth, 2005; van Haren et al., 1999).

Additional to the naturally occurring mixing processes, the increased interest in renewable energies and the development of the technology to build wind turbines offshore in greater water depths have led to the

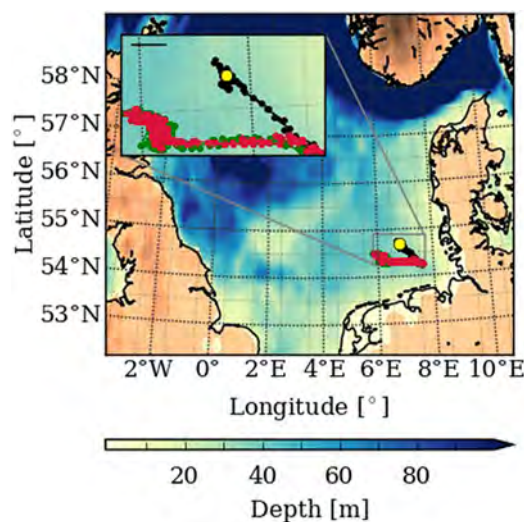


Figure 1. Research area of the campaigns in 2014 and 2015. Deployment location and flight paths of Amadeus (C14), Comet (C15), and Sebastian (C15) are shown in black, green, and red, respectively. All paths are situated within the German Bight of the North Sea. The location of the ADCP is marked by a yellow dot. The colormap represents the water depth in meters, which has been created using data from the National Centers for Environmental Information (NOAA, <http://maps.ngdc.noaa.gov/viewers/wcs-client/>). Water depths above 100 m are well outside the study area and are therefore not resolved in this map. The black overbar in the zoomed area indicates a distance of 20 km.

planning and construction of offshore wind farms (OWFs) at coastal regions (Carpenter et al., 2016; Ho et al., 2016). Turbine foundations generate additional turbulence in the water column that can contribute to mix a stratified regime. This additional mixing of the water column could alter nutrient levels and shift the competitive balance between phytoplankton species, altering phytoplankton growth and community composition, with possible implications for the marine food web and biogeochemical cycles (Carpenter et al., 2016; Franks, 2015; Huisman et al., 2004; Lauria et al., 1999). Results from an idealized study by Carpenter et al. (2016) suggest that OWFs could significantly impact stratification in the North Sea, given they are built in extensive areas of the shelf. Until 2015, 11 GW of offshore capacity had been installed in Europe, 69% of which is situated in the North Sea (Ho et al., 2016). Of the consented offshore wind farms, 78% of the total capacity is planned to be built in the North Sea, underlining the importance of this shelf sea for offshore development (Ho et al., 2016). To better understand the thermocline fluxes in seasonally stratified shelf seas, which could be altered by OWFs in the near future, the present paper focusses on quantifying turbulence and mixing in the German Bight region of the North Sea, as well as understanding the mechanisms responsible.

Two data sets of microstructure turbulence measurements collected in July–August 2014 and May–June 2015 over 12 and 17 days, respectively, are presented. To our knowledge, this is so far the most extensive data set of stratified turbulence in a shallow shelf sea. We analyze the dissipation

of turbulent kinetic energy in the German Bight region of the North Sea under strongly stratified to well-mixed conditions. Measurements were obtained by autonomous underwater gliders equipped with turbulence microstructure shear sensors. Underwater gliders have been shown to be suitable instruments to study turbulence as they move independently from ships or propellers, reducing the vibration noise in the shear probe measurements (Wolk & Lueck, 2009), and are able to reliably measure through long periods of time, even when subjected to adverse weather conditions (Fer et al., 2014; Palmer et al., 2015).

The following section provides an overview of the field measurements, including instrument deployment and relevant instrument details. Data processing is discussed in section 3, in which a description of the quality control of glider and microstructure measurements is included. In sections 4 and 5, results are presented and discussed, and in section 6 the paper is concluded providing insights on the mixing processes in the study area.

2. Overview of Field Measurements

To study turbulence and mixing in shallow shelf seas, measurements from two field campaigns conducted in the German Bight of the North Sea are presented (Figure 1). The first field campaign (C14) took place between 28 July 2014 and 18 August 2014. On 9 August, the Storm Bertha reached the studied region and was able to mix the water column thoroughly, drastically affecting the mixing conditions in the area. To concentrate on the mechanisms responsible for mixing under representative conditions, only the data collected before the storm (12 days) are analyzed. The sampling location was situated between 6.67°E, 54.26°N and 7.54°E, 54.76°N. Relevant instruments for this work are one Teledyne Webb Research Slocum Electric ocean glider (Amadeus) with a MicroRider-1000LP (MR, manufactured by Rockland Scientific International) mounted on its top and one acoustic Doppler current profiler (ADCP, RDI 600 kHz Workhorse Sentinel), which was mounted on the seafloor in 40 m water depth. The ADCP was positioned close to the buoy station Nordseeboje 3 (NSB3) at 54.68°N, 6.78°E and sampled horizontal velocities over nearly the whole water column range (5–38 m).

Further, within the studied period in 2014, we have conducted “spiral missions,” the beginning of which is indicated in Figure 5 by a dashed line between 4 and 5 August. During this period, the glider was

configured with a tail rudder position fixed to starboard, causing it to profile up and down in spirals with a diameter of about 10–12 m. In this setup, the glider moves horizontally with the mean velocity of the water column, which renders the parameters measured by the glider observed in an approximately Lagrangian fashion.

The second campaign (C15) was conducted between 21 May 2015 and 6 June 2015, in which two Teledyne Webb Research Slocum Electric ocean gliders (Comet and Sebastian) were deployed, each carrying a MR. The sampling area was located between 5.82°E, 54.24°N and 7.62°E, 54.52°N. The exact routes and instrument positions are shown in Figure 1.

All three gliders carried custom Sea-Bird Electronics conductivity, depth, and temperature sensors (Seabird SBE41 CTD) that measure at a frequency of 0.5 Hz. The gliders are further equipped with an attitude sensor (TCM3), an altimeter (AIRMAR Technology), a navigation pressure sensor (Micron Instruments, MP50–2000), an Iridium modem, and a global positioning system (GPS). On both campaigns, the gliders surfaced approximately every 3 h at which point the glider position is acquired via GPS. To reduce glider vibrations that can contaminate the shear probe measurements, the battery position was fixed for all gliders during upcasts and downcasts.

The MR, a microstructure instrument package, carried two orthogonally positioned air-foil shear probes (SPM-38, 512 Hz), two thermistors in C14 (FP07, 512 Hz) and one thermistor in C15 (FP07, 512 Hz), a pressure transducer (64 Hz), a vibration sensor (64 Hz), and an inclinometer (64 Hz).

3. Data Processing

3.1. Glider Dynamics and CTD Measurements

In contrast to vertical profilers, the glider moves through the water column in a sawtooth pattern. Hence, the speed along the microstructure sensors (U) cannot be obtained through the rate of change of pressure, but it needs to be estimated accounting for the glide angle. It is necessary to estimate U to obtain the dissipation of turbulent kinetic energy (ε) from shear probe measurements. Glider measurements are obtained from upcasts and downcasts, and understanding the flight behavior during these different casts is an active area of research. Therefore, since the procedure to calculate ε from microstructure shear sensors mounted on gliders is novel, and the conventions to process this type of data set are still under development, the present section describes the steps taken to obtain data for the scientific analysis.

Previous studies (e.g., Fer et al., 2014; Palmer et al., 2015) have used the hydrodynamic glider flight model of Merckelbach et al. (2010) to obtain U . The flight model assumes steady flight, that is, an equilibrium between buoyancy, drag, and lift forces, and takes the observed in situ density, measured pitch, and buoyancy drive as input parameters. The model yields the glider speed along the glide path and accounts for the angle of attack, a small, but nonzero angle between the glide angle and the pitch angle. Especially in stratified regions, however, the assumption of steady flight is questionable and the model results become less accurate. In order to retain the dynamic response of the glider due to sudden changes in forcing, for example, when passing a pycnocline, U is calculated from the depth rate, computed from the measured pressure, and the glide angle. Herein, the glide angle is composed of the measured pitch angle and the angle of attack, with the latter being computed using the steady state model. It is necessary to account for the effect of the angle of attack, as ignoring it could overestimate the glider speed through water by an amount of 2–4 cm s^{-1} (Merckelbach et al., 2010), or about 10% of the glider speed. Note that in this procedure it is tacitly assumed that the vertical water velocities are equal to zero.

Average values of pitch (θ), angle of attack (α), glider velocities (U), and vertical glider velocities (w_g) are shown in Table 1.

The conductivity signal measured by CTD sensors in the presence of sharp temperature gradients tends to be corrupted due to thermal lag effects in the conductivity cell (Lueck & Picklo, 1990). This in turn compromises the accuracy of salinity and therefore density estimates in thermoclines. General methods to correct for the thermal inertia have been proposed by, e.g., Lueck and Picklo (1990) and Morison et al. (1994). Correction methods for glider CTDs and, in particular, unpumped CTDs have been proposed by Garau et al. (2011). Nevertheless, due to the low sample rate of 0.5 Hz, the correction of the thermal lag effects turned out to be problematic for the current data set due to the sharp and strong thermocline present in C14.

Table 1
Average Values and 1 Standard Deviation of Flight Parameters (Glider's Along Path Velocity [U], Vertical Glider Velocity [w_g], Angle of Attack [α], and Pitch Angle [θ]) for Field Campaigns C14 and C15

Campaign/glider	Profile	U (m s ⁻¹)	w _g (m s ⁻¹)	α (°)	θ (°)
C14	Amadeus				
	Upcasts	0.36 (0.05)	-0.14 (0.05)	-3.46 (0.61)	-19.74 (3.81)
	Downcasts	0.21 (0.05)	0.08 (0.03)	3.33 (0.47)	21.00 (2.97)
C15	Comet				
	Upcasts	0.26 (0.04)	-0.11 (0.04)	-4.05 (0.50)	-21.70 (2.17)
	Downcasts	0.37 (0.04)	0.16 (0.05)	4.02 (0.45)	21.80 (1.96)
Sebastian	Upcasts	0.29 (0.03)	-0.12 (0.04)	-2.88 (0.28)	-23.86 (2.62)
	Downcasts	0.39 (0.04)	0.18 (0.06)	2.69 (0.23)	25.72 (2.38)

However, considering that the variance of the density profiles in the study area is dominated by temperature, we opted to apply a simplified technique for the calculation of density. Density is estimated as described in Carpenter et al. (2016), in which the accurate salinity estimates from the top and bottom mixed layers are used to calculate the change in density across the water column. Density profiles are then generated by using top and bottom density incremented by a proportional density contribution, which preserves the vertical shape of the temperature profiles.

3.2. Calculating the Dissipation of Turbulent Kinetic Energy

Estimates of U are used in the calculation of shear microstructure from the air-foil shear probes, from which the dissipation rates of turbulent kinetic energy are obtained. An air-foil shear probe detects velocity fluctuations perpendicular to its pointing direction by means of a piezo-ceramic beam that is able to sense a net force exerted by the cross-stream flow, producing an electric charge. Shear measurements are obtained using the measured voltage, the sensitivity of the shear probes, and the velocity of the glider (Lueck et al., 1990).

Assuming isotropic turbulence, the dissipation of turbulent kinetic energy can be calculated from the time series of one component of the shear tensor after a spectral analysis (fast Fourier transform), in which the variance of the spectra is estimated through the use of the Parseval theorem (described mathematically below in equation (1)). For the spectral analysis, a sample length of 12 s was chosen, and a total of five half-overlapping segments of 4 s each generated five shear spectra, which were averaged together for the calculation of one ε estimate. Thus, one ε estimate was obtained every 2–4.5 m horizontally and 0.95–2.5 m vertically on average, depending on the glide angle and on the glider along path velocity. Using Taylor's frozen turbulence hypothesis, it is assumed that the temporal rate of change of the quantity of interest is significantly less than its change attributed to spatial gradients, which enables the conversion of shear spectra in the frequency domain, Φ(f), into a spatial, wave number domain, Φ(k). For one ε_j estimate, a shear spectrum is integrated over a determined wave number range [k_{minj}, k_{maxj}]. The integrated values are multiplied by the kinematic viscosity of seawater ν, and a numerical scale factor to account for the assumption of isotropy (Lueck et al., 2002; Wolk et al., 2002):

$$\epsilon_j = \frac{15}{2} \nu \overline{\left(\frac{\partial u_j}{\partial x}\right)^2} = \frac{15}{2} \nu \int_{k_{minj}}^{k_{maxj}} \Phi_j(k) dk, \tag{1}$$

where the subscript j denotes the two different shear probes, and ε without subscript denotes the final dissipation estimates that are used in the scientific analysis.

The preliminary estimate of ε_j integrates the measured shear spectrum (Φ_j(k)) from the lowest available wave number (k_{minj}) to a maximum wave number (k_{maxj}), which is determined via an algorithm used to identify the spectral minimum through a polynomial fit (Lueck, 2013). This range of integration is chosen to eliminate contamination from instrumental noise at high frequencies. Based on this preliminary estimate, the integration range is iteratively adjusted by comparing the shear spectrum with the fitted form of the Nasmyth spectrum (Wolk et al., 2002). The upper limit of integration, k_{maxj}, is increased (decreased) if the shear spectrum is well above (below) the theoretical Nasmyth spectrum. In general, the higher (lower)

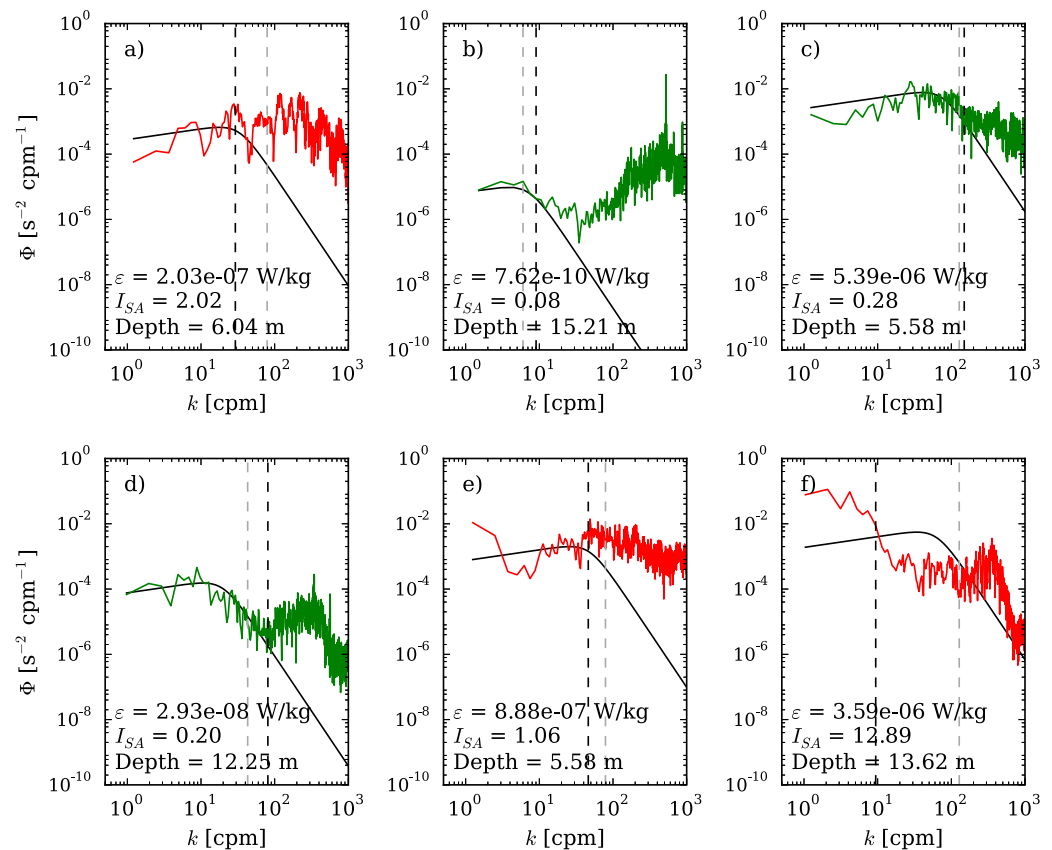


Figure 2. Shear spectra (red and green lines) and their corresponding empirical Nasmyth spectra (black line). The black and gray dashed lines correspond to k_{max} and k_{noise} , respectively. The color green stands for shear spectra that passed I_{SA} , whereas red indicates a bad agreement between the shear spectrum and the empirical spectrum identified by the index. The corresponding ϵ estimate, I_{SA} , and depth are included in each plot.

the quality of the shear spectra obtained, the closer (farther apart) k_{max} is going to be to the wave number at which the spectrum ceases to roll-off and is dominated by instrumental noise (k_{noise} , Figure 2). The k_{noise} wave number has been observed to vary among different orders of magnitude of ϵ (Bluteau et al., 2016; Fer et al., 2014; Nasmyth, 1970) and was determined here by averaging the shear spectra over the complete data set in bins of ϵ (for reference, see Figure 9 in Fer et al., 2014).

Interferences in the shear signal may occur due to motions of the glider. To account for this, the algorithm suggested by Goodman et al. (2006) was used prior to the evaluation of the quality of the shear spectra and the estimation of dissipation. Differences in ϵ estimates obtained with and without the use of the Goodman algorithm were on average within a factor of 2 and are presented in section 3.4. Furthermore, to ensure that only high-quality data would be included in the scientific analysis, several steps were taken to monitor the measurements, which are described in the following subsection.

3.3. Identification of Reliable ϵ Estimates and Criteria for Data Selection

In the following, we discuss the steps taken to control the quality of the acquired data, including a discussion on the glider velocities through water, vertical velocities, and the quality of the measured shear spectra.

Due to the intermittency of turbulence and other sources of error, shear spectra are not expected to agree perfectly with the empirical Nasmyth spectra (Fer et al., 2014). To distinguish dissipation estimates generated from shear spectra that considerably deviate from the empirical Nasmyth spectra from the estimates

generated by well-fitting spectra in an automated manner, we propose the empirically defined index of spectral agreement:

$$I_{SA} = \left[\frac{1}{n} \cdot \sum_{i=1}^n \log^2_{10} \left(\frac{\Phi_{SH_i}}{\Phi_{N_i}} \right) \right]^{1/2} \cdot \frac{k_{noise}}{k_{max}}, \tag{2}$$

where Φ_{SH_i} and Φ_{N_i} correspond to the shear spectrum and the corresponding value from the fitted Nasmyth spectrum, which are compared against each other from k_{min} ($i = 1$) until k_{noise} ($i = n$). In equation (2), subscript j has been dropped for convenience. The factor with the square root in equation (1) corresponds to a normalized root-mean-squared error between the shear and Nasmyth spectra in logarithmic space, whereas the second factor assesses the bandwidth of the shear spectra by comparing k_{noise} to k_{max} . The lower the value of I_{SA} , the better the agreement with the Nasmyth spectrum is expected to be. By manually comparing the spectra with I_{SA} , a threshold $I_{SA} < 1$ was found to effectively reject “low-quality” spectra (e.g., Figure 2).

From the previous subsection, we know that two independent values of ϵ are generated simultaneously as a result of the orthogonally positioned shear sensors. These two different ϵ_j estimates are averaged together if they agree up to a factor of 4. Otherwise, the ϵ_j estimate whose shear spectrum is in closest agreement with its respective Nasmyth spectrum is chosen. If the shear spectra from both estimates are of bad quality, the estimate is annulled. Dissipation estimates above $10^{-5} \text{ W kg}^{-1}$ were mainly characterized by overly noisy spectra, whereas dissipation estimates below $10^{-11} \text{ W kg}^{-1}$ were related to spectra with extremely weak curvature, in which the transition from the inertial subrange to the dissipation range could be barely detected. Therefore, for $\epsilon_j < 10^{-11} \text{ W kg}^{-1}$ and for $\epsilon_j > 10^{-5} \text{ W kg}^{-1}$, dissipation estimates were not considered in the scientific analysis. In total, the amount of rejected ϵ associated with unreliable shear spectra was below 6% for all gliders, which points to the high quality of the data collected.

The validity of the assumption of Taylor’s hypothesis of frozen turbulence in the calculation of ϵ and the implications of notably high or low vertical glider velocities have been amply discussed by Fer et al. (2014) and is briefly addressed in this subsection. When discussing glider velocities in the context of the estimates of dissipation of turbulent kinetic energy, U and the vertical glider velocity, w_g , have been averaged over the sample length used for producing an ϵ estimate.

To test the ϵ estimates against Taylor’s hypothesis, a threshold value of $U \geq 20u_t$ was chosen for upcasts and downcasts based on the same analysis performed by Fer et al. (2014), where u_t is defined as the turbulent velocity scale (cf. Appendix A). In our data set, high values of the angle of attack did not seem to affect directly the dissipation rates. Therefore, we set a limit of $|\alpha| < 20^\circ$, which is the standard value suggested by the manufacturers for the proper functioning of the air-foil shear probes (Lueck, 2013). As in Fer et al. (2014), the thresholds for vertical velocities were set to a minimum of 0.04 m s^{-1} and a maximum of 0.5 m s^{-1} . As an example, after data processing, Amadeus (C14) had 3.4% of its data points removed in the upcasts, 9.6% of which were rejected for failing Taylor’s hypothesis. A total of 52,528 data points collected

Table 2
Total Number of Data Points Available for Scientific Analysis After Data Processing and Percentage of Rejected Values (C14 and C15)

Campaign/ glider	Profile	Total number of data points after processing	Total of data points rejected (%)	Percentage rejected due to $U \leq 20 \text{ ut}$	Percentage rejected due to I_{SA}
C14 Amadeus	Upcasts	52,528	3.4	9.6	90.4
	Downcasts	83,520	6.3	52.3	46.0
C15 Comet	Upcasts	107,440	4.5	77.6	21.8
	Downcasts	76,339	1.4	50.1	45.9
Sebastian	Upcasts	113,202	1.8	57.9	40.3
	Downcasts	77,018	0.9	39.7	54.4

during Amadeus' upcasts were left for scientific analysis. The percentages of the rejected data for all gliders are listed in Table 2.

3.4. Agreement Between ϵ Estimates From Upcasts and Downcasts and Different Gliders

The mean agreement between the estimates of ϵ obtained from upcasts and downcasts was a factor of 2.1 for Amadeus, 1.1 for Comet, and 1.0 for Sebastian. In view of the good agreement between upcasts and downcast measurements from Amadeus during C14, these estimates were analyzed together in the generation of mean vertical profiles to enhance statistical significance (Figure 3). Differences in ϵ estimates observed between upcasts and downcasts of single gliders appear to be related to the flight behavior of the glider and the extent to which the method applied is able to describe it. For example, small errors in the measured pitch or in the angle of attack obtained by the hydrodynamic flight model could be responsible for the imperfect agreement between the casts.

During C15, inferences of dissipation of turbulent kinetic energy from Comet's and Sebastian's upcasts and downcasts agreed on average by a factor of 3.6–6.9. In C15, the data sets were collected in early spring by two different gliders that were approximately 15.4 (± 10) km apart, and consequently subjected to elevated spatial variability of turbulent events due to unsteady and patchy weak vertical stratification. Therefore, upcasts and downcast measurements from Comet and Sebastian are considered to be in very good agreement and were evaluated together when producing averaged profiles (Figure 3).

Figure 4 shows the probability distributions of ϵ inferred from shear measurements during upcasts and downcasts for all three gliders. Results are shown with and without the use of the Goodman algorithm (Goodman et al., 2006), which is used to remove the influence of glider motions on the shear measurements. Estimates obtained after using the algorithm differed on average by a factor of 0.6–0.8 from the raw estimates. Even though there is a risk of underestimation of turbulence by the use of the Goodman algorithm (Fer et al., 2014; Palmer et al., 2015), a factor of two difference between the estimates is within the acceptable uncertainty range, as ϵ varies by many orders of magnitude.

In the following, the temporal and vertical variability of ϵ and related quantities are introduced and discussed. Descriptive statistics are used to present the data, whereby mean values of turbulent parameters (ϵ ,

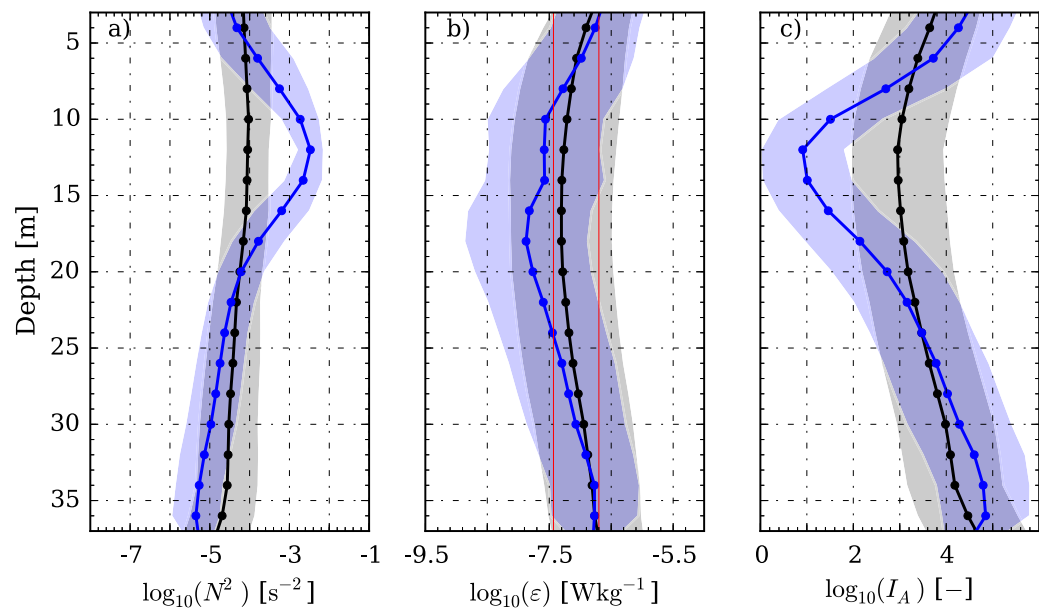


Figure 3. Vertical profiles of the decadic logarithm of the mean and 1 standard deviation of (a) N^2 , (b) ϵ , and (c) I_A . The mean of the data at every two meters was determined for the complete stratified period of the campaign in 2014 (C14, blue data points) and during the complete research cruise in 2015 (C15, black data points). Shaded blue and black areas represent 1 standard deviation of the corresponding values during C14 and C15, respectively. In Figure 3b, the red lines represent the lower and upper estimates of additional turbulence that could be supplied to the water column by the large-scale installation of offshore wind farm foundations in the North Sea.

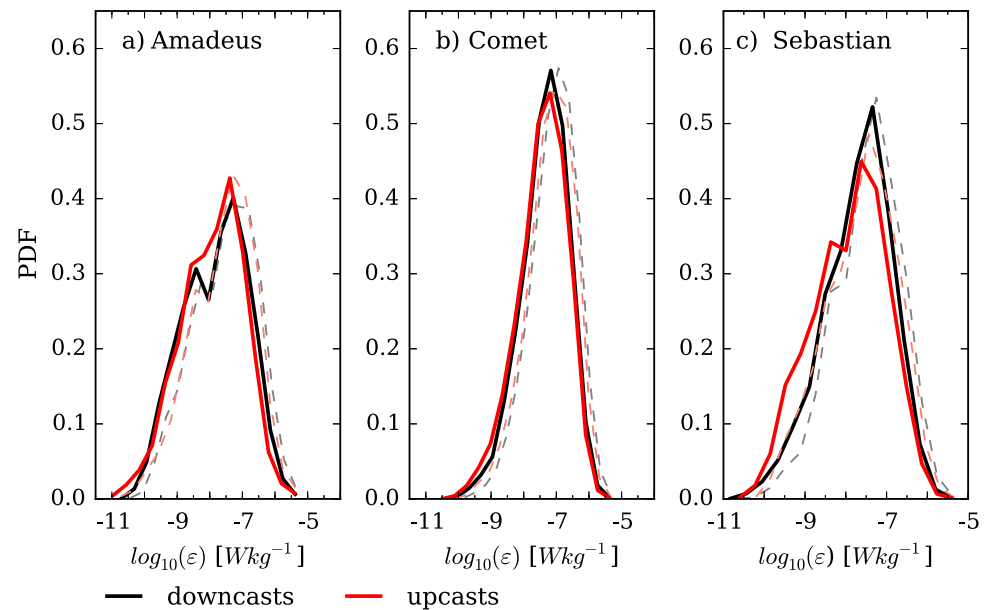


Figure 4. Probability density functions (PDFs) of the decadic logarithm of the dissipation of turbulent kinetic energy estimates from upcasts (red, solid lines) and downcasts (black, solid lines) after applying the Goodman algorithm (Goodman et al., 2006). Red and black dashed lines correspond to the PDFs of the dissipation estimates without the use of the algorithm for upcasts and downcast, respectively. (a) Amadeus, (b) Comet, and (c) Sebastian.

K_p, I_A, N^2) were calculated after Baker and Gibson (1987) assuming a lognormal distribution. The interquartile range is defined as the range between the 25th and the 75th percentiles.

4. Results

4.1. Stratification and the Dissipation of Turbulent Kinetic Energy

In C14, the water column in the research area was strongly stratified, with a $5.0 (\pm 2.2)$ m thick thermocline situated between $10.3 (\pm 1.7)$ m and $15.2 (\pm 1.5)$ m depth on average (± 1 standard deviation). The difference in temperature between surface and bottom mixed layers was approximately $\Delta T = 6^\circ\text{C}$, whereby the water temperature in these layers was around $20\text{--}21^\circ\text{C}$ and $14\text{--}15^\circ\text{C}$, respectively, for all of the C14 data presented (Figure 5a). Here the thermocline depth and thickness are calculated by first sorting each temperature profile to be monotonically decreasing with depth to circumvent temperature overturns. Subsequently, the temperature at the top and bottom of the main thermocline are defined as being $0.1\Delta T$ ($\sim 0.6^\circ\text{C}$) warmer (bottom) or cooler (top) than mixed layer temperatures (Figure 5a, thin black lines). Unless specified otherwise, we refer to this definition of the thermocline throughout the study. Note that, however, a second, much weaker, thermocline is observed with a temperature difference of $0.05\Delta T$ ($\sim 0.3^\circ\text{C}$) between thermocline extremities and bottom mixed layers (Figure 5a, red lines).

A tidal amplitude of approximately 0.4 m s^{-1} was recorded during C14. In the North Sea, semidiurnal tides are major contributors of variance in currents, which travel in a counterclockwise direction along the coasts and have the largest amplitudes along the eastern English and German coasts (Huthnance, 1991). The ϵ estimates reveal a clear tidal signal in the bottom mixed layer from tidally driven bottom boundary layer turbulence (Figure 5b). The tidally driven turbulence in the lower layer is damped by the stable stratification in the thermocline throughout the presented period, thus bottom boundary layer turbulence is not observed within the thermocline nor in the surface mixed layer. In the surface mixed layer, high values of ϵ are observed toward the water surface and are largely explained by wind forcing. Within the thermocline, turbulence is sporadic and ranges between 2.7×10^{-11} and $9.8 \times 10^{-6} \text{ W kg}^{-1}$, with a mean of $2.0 \times 10^{-8} \text{ W kg}^{-1}$ (Figure 5b and Table 3). Dissipation rates were the highest at the surface mixed layer and bottom boundary layer. The lowest dissipation levels occurred at the center of the thermocline and below it. Figure 6 depicts the vertical variability of the dissipation estimates and the squared buoyancy frequency with

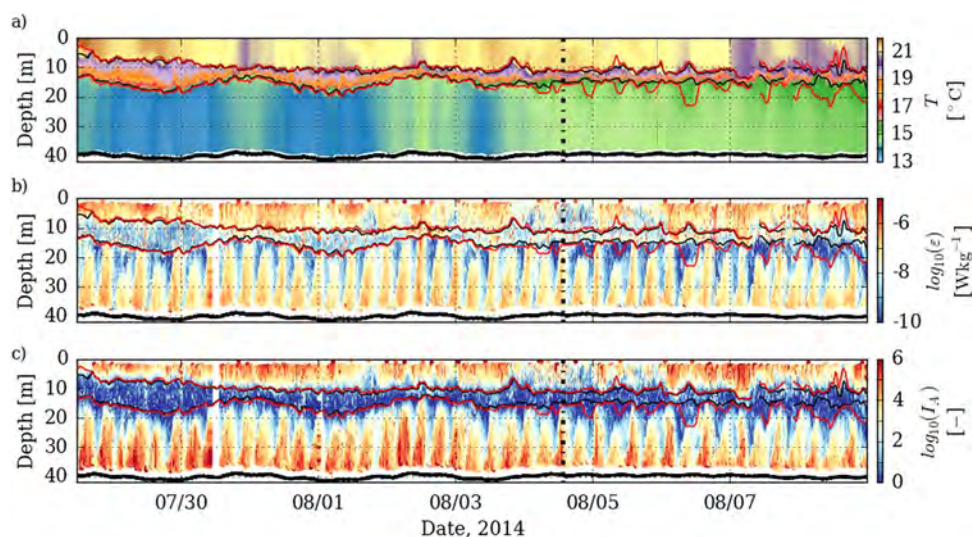


Figure 5. Time series of (a) temperature, (b) ε , and (c) I_A during C14. The main thermocline is shown in black together with a second, less sharp, thermocline (red line) for comparison. The thick black line in the bottom (around 40 m) delineates the seabed. The black dot-dashed lines show the start of the “spiral missions,” in which the position of the tail rudder of the glider was fixed (more details in sections 2 and 5.1). These scatterplots were produced using measurements and estimates derived from upcasts (Amadeus).

respect to the center of the thermocline. Even though ε estimates were overall lower within the thermocline than in the mixed layers, they were relatively higher in the extremities of the thermocline than in its center (Figures 3 and 6).

In C15, the water column remained well mixed for the majority of the time. The strong tidal signature can be clearly visualized in the dissipation estimates and, in the absence of significant vertical stratification, nearly reaches the top of the water column (Figure 7b). The highest ε values were observed near the sea surface and the seabed, whereas the lowest ε estimates were obtained during slack water periods at mid-water depths. Minimum and maximum ε were 1.5×10^{-11} and $9.6 \times 10^{-6} \text{ W kg}^{-1}$, and the mean was $8.3 \times 10^{-8} \text{ W kg}^{-1}$ (Table 3). Both gliders captured the onset of stratification in the end phase of the campaign, approximately 3 days before the end of the research cruise. During these days, the temperature difference between surface and bottom mixed layers reached 1°C . Moreover, in 23–28 May, both gliders recorded data from an unsteady and weakly stratified area, in which the net temperature change between surface and bottom mixed layers was most often below 0.5°C and occasionally as low as 0.2°C . In this period, the weak stratification is observed to damp the tidally driven bottom boundary layer turbulence, which is trapped below the temperature gradient (Figure 7b). While the wind speed during this period remained below 10 m s^{-1} , on 28 May, the wind speed reached 12.5 m s^{-1} and was able to effectively mix the weak stratification.

Table 3

Qualitative Statistics of the ε Estimates for the Whole Water Column and the Thermocline

	2014		2015
	Thermocline	Water column	Water column
Minimum	2.7×10^{-11}	1.1×10^{-11}	1.5×10^{-11}
Maximum	9.8×10^{-6}	9.9×10^{-6}	9.6×10^{-6}
Mean	2.0×10^{-8}	6.3×10^{-8}	8.3×10^{-8}
Median	5.5×10^{-9}	2.7×10^{-8}	4.7×10^{-8}
25th	1.7×10^{-9}	3.8×10^{-9}	1.1×10^{-8}
75th	3.0×10^{-8}	1.2×10^{-7}	1.5×10^{-7}

Note. Mean values have been calculated after Baker and Gibson (1987) assuming a lognormal distribution. The 25th and the 75th percentiles are given under 25th and 75th, respectively. All values are reported in W kg^{-1} .

4.2. Turbulent Activity Index

The turbulent activity index, I_A , is used to quantify turbulent mixing under stratified conditions. The I_A can be obtained from the ratio of the Ozmidov scale (L_O) to the Kolmogorov scale $L_K = (v^3/\varepsilon)^{1/4}$, that is, the ratio of the largest possible turbulent eddies given the strength of the stratification ($N^2 = (g/\rho_0)d\rho/dz$, the buoyancy frequency squared) and the smallest viscous scales in turbulent flow, which depend only on ε and ν (Hebert & de Bruyn Kops, 2006),

$$I_A = \left(\frac{L_O}{L_K} \right)^{4/3} = \frac{\varepsilon}{\nu N^2}. \quad (3)$$

Figures 5c and 7 show the areas characterized by a high and low turbulent activity index. Experimental and numerical analysis suggest

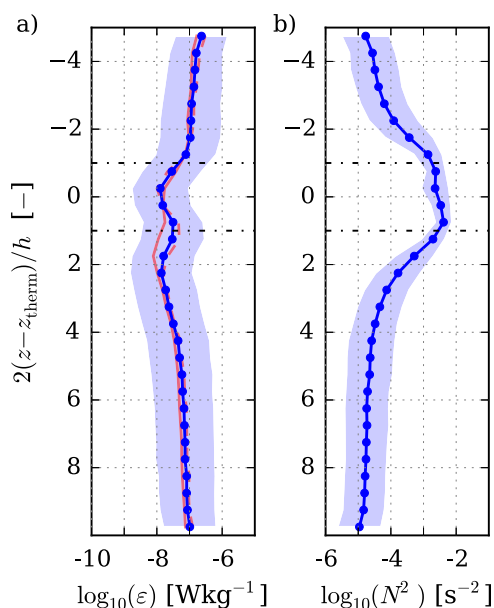


Figure 6. Vertical profiles of the decadic logarithm of the mean (blue) and 1 standard deviation (blue shade) of (a) ϵ and (b) N^2 . The calculations refer to the complete stratified period of the campaign (C14), whereby the data were centered with respect to the nondimensionalized main thermocline found between -1 and 1 . In the y axis, z_{therm} represents the center of the thermocline and h is the thermocline thickness. Time-averaged vertical profiles of upcasts and downcasts in C14 are depicted by the continuous and dashed red lines, respectively.

that fully turbulent isotropic mixing takes place when $I_A > O(10^2)$ (Shih et al., 2005; Smyth & Moun, 2000). During C14 (C15), 69% (81%) of the I_A estimates were higher than the threshold value 100, indicating fully turbulent and isotropic mixing for the majority of the collected data points. However, within the thermocline the interquartile range of I_A was 0.6–7.2, and only 6% of the data points resulted in a I_A above 100, suggesting a regime shift within the thermocline. A total of 20% of the data points in the thermocline were found between $7 \leq I_A \leq 100$, the transitional regime, in which turbulence is able to actively mix stratification despite not being fully isotropic (Bouffard & Boegman, 2013; Shih et al., 2005; Stillinger et al., 1983).

A turbulent activity index lower than 7–20 indicates quiescent flow, being therefore not sufficiently energetic to promote significant diapycnal mixing (Itsweire et al., 1986; Ivey et al., 2008; Stillinger et al., 1983). Within the quiescent level, Bouffard and Boegman (2013) have suggested a differentiation between a molecular regime and a buoyancy-controlled regime by extending existing parameterizations based on a low Prandtl number $Pr = 0.7$ (Shih et al., 2005) to higher Prandtl numbers up to 700. The Prandtl number denotes the ratio of momentum to the scalar diffusivities. By considering $0.7 \leq Pr \leq 700$, the corresponding value for the diffusion of heat in seawater $Pr_{\text{sw}} \approx 7$ (at 20°C) is included. In the molecular regime, $I_A < 10^{2/3} Pr^{-1/2}$ ($I_A < 1.7$ at Pr_{sw}), turbulence is expected to be completely suppressed by stratification, resulting in laminar flow. In the buoyancy-controlled regime $10^{2/3} Pr^{-1/2} \leq I_A \leq (3 \ln \sqrt{Pr})^2$ ($1.7 < I_A < 8.5$ at Pr_{sw}), turbulent mixing takes place, albeit at much lower rates than in the intermediate regime. Within the thermocline (C14), approximately 77% of

the I_A estimates were below 8.5, of which 67% were lower than 1.7. Therefore, in contrast to the bottom and surface mixed layers, the thermocline is characterized by quiescent to transitional flow.

Figure 8 depicts three different levels of I_A in the thermocline, defined by Shih et al. (2005): (1) quiescent or laminar (blue dots, $I_A < 7$), (2) intermediate between quiescent and turbulent flow (yellow dots,

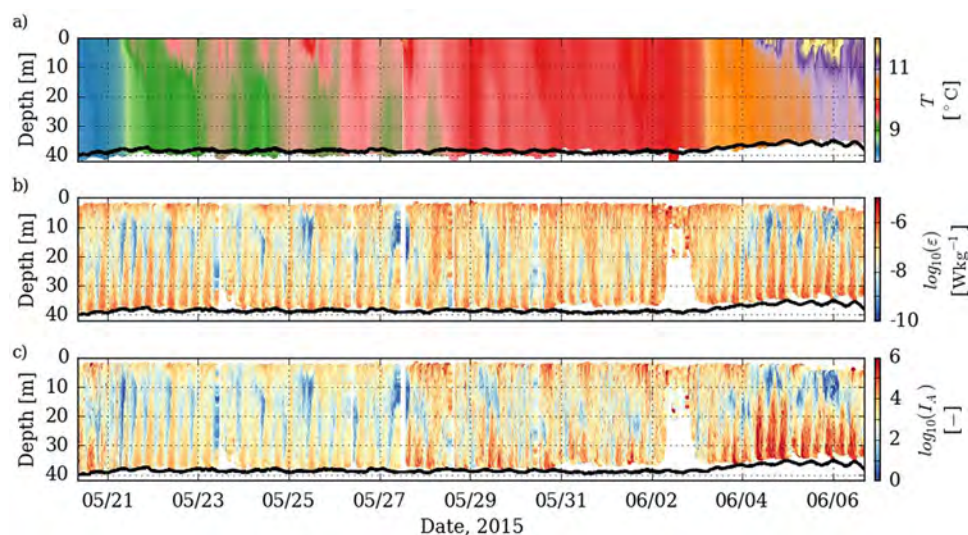


Figure 7. Time series of (a) temperature, (b) ϵ , and (c) I_A during C15. The thick black line in the bottom (around 40 m) delineates the seabed. These scatterplots were produced using measurements and estimates derived from upcasts (Comet).

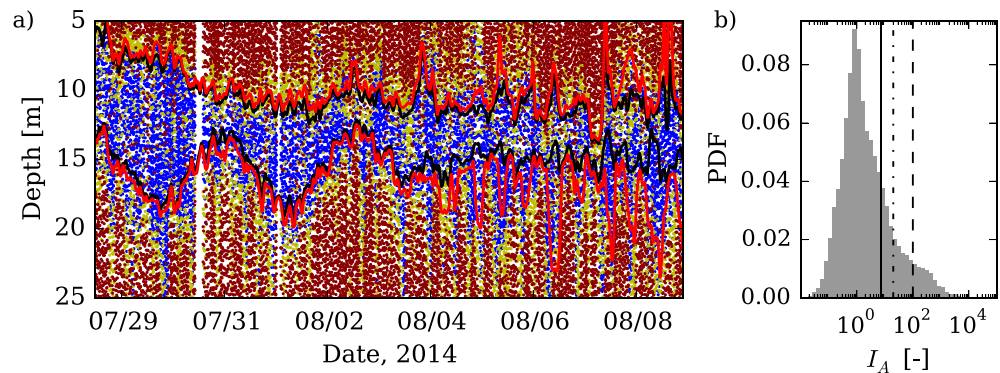


Figure 8. (a) Turbulent activity index at the thermocline (C14). Red dots represent $I_A > 100$, yellow dots stand for $7 \leq I_A \leq 100$, and blue dots symbolize $I_A < 7$. The black and red lines delineate the main and secondary thermoclines, respectively. (b) Histogram of I_A in the main thermocline. The solid line indicates $I_A = 7$, the dot-dashed line holds the $I_A = 20$ mark, and the dashed line shows $I_A = 100$.

$7 \leq I_A \leq 100$) and (3) fully turbulent flow (red dots, $I_A > 100$). The extremities of the thermocline are dominated by quiescent flow, which occasionally develops into turbulence.

4.3. Turbulent Diffusivity in the Thermocline

Within the thermocline, the intensity of diapycnal mixing generated by the observed values of dissipation of turbulent kinetic energy is estimated by using the Osborn relation for every ε estimate:

$$K_p = \Gamma \frac{\varepsilon}{N^2}, \quad (4)$$

where Γ is the so called “mixing efficiency.” Γ has been frequently set to 0.2 for shear-generated mixing (Osborn, 1980; Thorpe, 2007), although more recent studies reporting on direct numerical simulations (Shih et al., 2005) and oceanic field measurements (Walter et al., 2014) define $\Gamma = f(I_A)$.

Parameterizations of variable mixing efficiency commonly set $\Gamma = 0.2$ for the intermediate regime defined in subsection 4.2, and $\Gamma = 2N(v/\varepsilon)^{1/2}$ for the fully turbulent regime, with the mixing efficiency approaching zero as I_A increases (Bouffard & Boegman, 2013; Ivey et al., 2008; Shih et al., 2005). For the buoyancy-controlled regime, the mixing efficiency is calculated as $\Gamma = 0.1\varepsilon^{1/2}/(Pr^{1/4}v^{1/2}N)$ and, in the molecular regime ($I_A < 1.7$), K_p is set to $1.4 \times 10^{-7} \text{ m}^2 \text{ s}^{-1}$ (Bouffard & Boegman, 2013), which corresponds to the molecular diffusion coefficient of heat in seawater (κ_T).

In the following, we present results from both parameterizations, of which differences will be shown in subsection 5.1 to significantly affect the rate of vertical scalar flux, and therefore the heat budget. The estimated turbulent diffusivity levels spanned over several orders of magnitude within the thermocline, namely over 10^{-7} – $10^{-4} \text{ m}^2 \text{ s}^{-1}$ for $\Gamma = f(I_A)$ and over 10^{-7} – $10^{-2} \text{ m}^2 \text{ s}^{-1}$ for a constant mixing efficiency. Turbulent mixing was in general relatively low, with the interquartile range of the turbulent diffusion rate between 1.4×10^{-7} and $2.0 \times 10^{-6} \text{ m}^2 \text{ s}^{-1}$ for both parameterizations. In this region of the water column, K_p was often close to the molecular diffusion coefficient of heat in seawater, which was expected as a considerable portion of the thermocline is dominated by the laminar regime (cf. subsection 4.2). Higher mixing rates on the order of $O(10^{-5})$ – $O(10^{-4}) \text{ m}^2 \text{ s}^{-1}$ were found in the upper half of the thermocline and, during ebb and flood periods, in the bottom of the thermocline where it encounters the bottom mixed layer. The turbulent mixing rates obtained in this study are in reasonable agreement with other studies (Burchard & Rippeth, 2009; Ledwell et al., 2004; Palmer et al., 2015; Rippeth, 2005; van Haren et al., 1999) and are discussed in the following section by means of the calculation of the heat budget.

5. Discussion

On both campaigns, high dissipation levels were observed close to the water surface and near the seabed, which is explained by enhanced turbulence caused by wind and bottom friction of the tidal currents, respectively. Dissipation estimates obtained during slack water at midwater depths were about 2

orders of magnitude lower than during periods of tidal motion. The tidal signature in ε extended upward until the thermocline in the stratified data set (C14), and until a height of 25–30 m in the well-mixed areas in C15. These observations are in good agreement with Simpson et al. (1996), who conducted measurements in 1993 in the Irish Sea over a few tidal periods, and with Palmer et al. (2008), who reported on measurements taken in 2003 in the Celtic Sea. Within the thermocline, turbulence varied over several orders of magnitude, underlining the difficulty in estimating a mean value for the dissipation of turbulent kinetic energy.

Further, it was observed in C15 that a temperature difference of 0.2°C is able to damp boundary-generated ε , decreasing the turbulent activity to transient and quiescent levels, and therefore suppressing vertical fluxes for the given time period (Figure 7). Measurements obtained from both gliders during C15 revealed that in early spring, before a steady thermocline is established, turbulence and stratification properties in the studied region are highly variable.

5.1. Stratification and Transport Through the Thermocline

To investigate the role of the thermocline in limiting transport between layers, we use glider measurements taken during the “spiral missions” introduced in section 2, in which the glider moves in an approximately Lagrangian fashion and is therefore expected to remain in the same body of water. The spiral missions were conducted close to the bottom-mounted ADCP and took place under light wind conditions, on average 5.2 (± 2.2) m s^{-1} . Therefore, given that the geographical variation of the glider during the spiral missions was low (8.3 km), horizontal advection of heat is expected to play a minor role and is neglected. Furthermore, the average temperature within the water column in this period was conserved at 17 (± 0.2)°C, which further suggests that solar heating and heat absorption through the seabed can be neglected, enabling the calculation of the heat budget.

5.1.1. Heat Budget

The estimates of dissipation of turbulent kinetic energy obtained during the spiral missions are shown in Figure 9. The mean vertical heat flux $\langle Q_T \rangle$ (W m^{-2}) is estimated for each profile using the heat capacity of seawater $c_p = 3,993 \text{ J kg}^{-1} \text{ K}^{-1}$ at 20°C, the mean of the depth derivative of temperature within the thermocline limits $\langle \partial T / \partial z \rangle$ and the depth-averaged thermocline turbulent diffusivity K_{thm} :

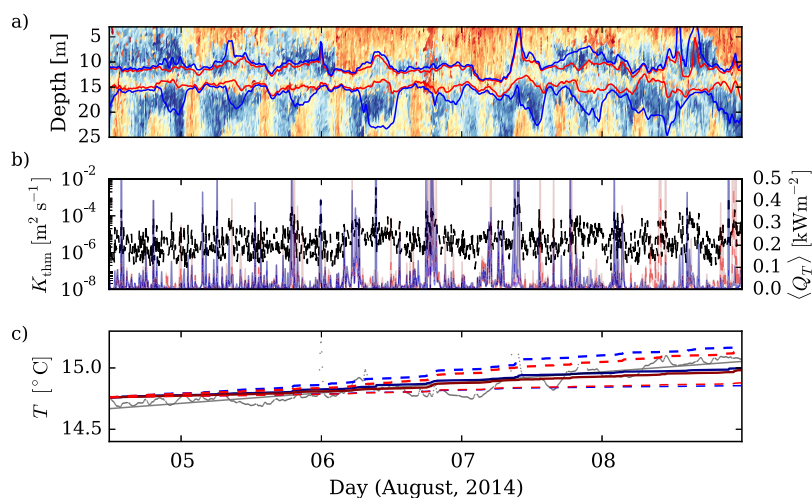


Figure 9. (a) ε estimates during the spiral missions conducted in the C14 campaign. The thin lines around 10 and 15 m indicate the position of the thermocline, where red and blue lines stand for the thermocline definitions (i) and (ii), respectively. This scatterplot was produced using measurements from upcasts (Amadeus). (b) Average turbulent diffusivity ($\Gamma=0.2$) within the main thermocline (black dashed line). The continuous lines show the vertical heat flux calculated with $\Gamma=0.2$, whereby the red line shows results for the thermocline definition (i) and, conversely, the blue line shows results from definition (ii). (c) Measured evolution of bottom mixed layer temperature with time (black dots). The black line corresponds to a linear regression of the measured data points. The parameterized increase in bottom mixed layer temperature is depicted by continuous lines (constant Γ), thin dashed lines (variable Γ), and thick dashed lines (ε calculated without the Goodman algorithm, with constant Γ). The line colors have the same meaning as described in Figure 9a. This analysis was conducted using measurements taken during the spiral missions (4–9 August) in C14.

Table 4
Overview of the Heat Budget Performed During the Spiral Missions in C14

Case	$\langle Q_T \rangle$ (W m^{-2})	dT/dt ($^{\circ}\text{C s}^{-1}$)	Percentage explained through K_{thm} (%)
$\varepsilon, \Gamma=0.2, G$	44.8–49.5	$6.1\text{--}6.8 \times 10^{-7}$	64.3–73.5
$\varepsilon, \Gamma=0.2$	79.8–84.3	$1.0\text{--}1.2 \times 10^{-6}$	111.1–126.7
$\varepsilon, \Gamma=f(I_A), G$	18.5–25.7	$2.8\text{--}3.2 \times 10^{-7}$	29.6–34.2
$\varepsilon, \Gamma=f(I_A)$	29.3–41.4	$4.4\text{--}5.3 \times 10^{-7}$	47.0–55.6

Note. The space and time averages of the heat flux $\langle Q_T \rangle$ across the thermocline and of the rate of change in bottom mixed layer temperature dT/dt are listed for the studied cases. Similarly, the percentage of the heat budget that can be explained through the estimated thermocline turbulent diffusivity K_{thm} is reported. In the description of the cases, the letter “G” denotes the use of the Goodman algorithm in the calculation of the ε . The range shows the variation among different thermocline definitions

$$\langle Q_T \rangle = \rho_0 c_p K_{thm} \left\langle \frac{\partial T}{\partial z} \right\rangle, \tag{5}$$

where K_{thm} is calculated as

$$K_{thm} = \frac{1}{h} \int_{h_{top}}^{h_{bot}} K_p dz, \tag{6}$$

in which h_{top} and h_{bot} stand for the thermocline limits, and h is the thermocline thickness. In equation (5), it is observed that the K_{thm} factor largely determines the outcome of the heat flux as, in contrast to $\langle \partial T / \partial z \rangle$, it varies over several orders of magnitude.

There is no universal definition of the thermocline, which is a source of uncertainty when estimating the heat budget. To account for this uncertainty, we calculate the heat budget based on the two different definitions of the thermocline given in section 4. Moreover, the bottom and top of the thermocline are marked either by (i) $0.1\Delta T$, or (ii) $0.05\Delta T$ lower (higher) temperatures than in the top (bottom) mixed layers. Depending on the definition of the thermocline and the Γ parameterization used, the average vertical heat flux driven by diapycnal turbulent diffusion between 4 and 9 August was $18.5\text{--}49.5 \text{ W m}^{-2}$ (Table 4). The depth-averaged thermocline turbulent diffusivity K_{thm} and the vertical heat flux are depicted in Figure 9b. During this period, the temperature in the bottom mixed layer increased by 0.4°C , which corresponds to a warming rate of $1 \times 10^{-6} \text{ }^{\circ}\text{C s}^{-1}$. The predicted effect of $\langle Q_T \rangle$ on the bottom mixed layer temperature was calculated as

$$\frac{dT}{dt} = \frac{\langle Q_T \rangle}{c_p \rho_0 H}, \tag{7}$$

where dT/dt is the rate of change of temperature ($^{\circ}\text{C s}^{-1}$), and H (m) is the height of the bottom mixed layer (BML). The measured increase in BML temperature based on definition (i) is depicted in Figure 9c, alongside with the estimated change in BML temperature due to diapycnal diffusion (equation (5)). Depending on the two definitions of the thermocline described above, and on the definition of the mixing efficiency, the parameterized vertical heating rate was on average $2.8 \times 10^{-7}\text{--}6.8 \times 10^{-7} \text{ }^{\circ}\text{C s}^{-1}$ (Table 4). Moreover, 30–74% of the observed increase in bottom mixed layer temperature could be traced back to diapycnal mixing generated from turbulence within the thermocline (Table 4). A steady state heat budget estimate, in which K_{thm} and dT/dz were set constant from the average over the spiral missions, shows that 14–62% of the increase in bottom mixed layer temperature can be attributed to above average thermocline turbulent diffusivities. Approximately 26–69% of the parameterized increase in temperature can be traced back to high heat flux rates ($\langle Q_T \rangle \geq 80 \text{ [W m}^{-2}\text{]}$), suggesting that much of the heating of the bottom mixed layer is triggered by sporadic events of high turbulent diffusivity (Figure 9). This also highlights the need for long uninterrupted time series to accurately capture turbulent fluxes.

5.1.2. Considerations

Possible errors in the calculation of ε , and therefore of K_{thm} , may explain the difference between measured and calculated flux rates (Palmer et al., 2008; Simpson et al., 1996) as ε estimates are uncertain within at least a factor of 2. Estimates of the dissipation of turbulent kinetic energy from gliders have relied until

recently on instrument velocities calculated either through the hydrodynamic flight model introduced in section 3, or through the vertical velocity, the pitch angle and the angle of attack. As shown in Figure 6a, the agreement between upcasts and downcasts in the time-averaged vertical profiles is largely within a factor of 2, with the exception of the bottom of the thermocline. In the bottom of the thermocline, the time averages of upcasts and downcasts agree by a factor of 2.6–4.4. Further research on the glider flight is needed to advance current understanding of its behavior when entering and leaving sharp thermoclines, and therefore reducing the uncertainties when calculating ε . The addition of recently developed velocimeters for microstructure packages might help to improve current understanding of the glider flight. Another source of uncertainty is the use of the Goodman algorithm in the calculation of ε , which might not be appropriate when using gliders (Fer et al., 2014; Palmer et al., 2015). If K_p is estimated using ε without the Goodman algorithm, the increase in BML temperature can be traced back to vertical mixing is a factor of 0.5–1.3 of the measured temperature change (Table 4).

Further, the choice of applying a constant mixing efficiency $\Gamma=0.2$ instead of $\Gamma=f(I_A)$ in the calculation of K_p has a significant effect in closing the heat budget. The parameterization based on a constant mixing efficiency significantly improves the recovery of the heat budget compared to a mixing efficiency that varies with the turbulence activity index (Figure 9b). These results suggest that the experimentally defined constant mixing efficiency might still be more accurate than the parameterization relating the mixing efficiency with the turbulent activity index, as already suggested by Gregg et al. (2012) and Cyr et al. (2015). Overall, these results underline the importance of diapycnal mixing for heat transfer into deeper layers of the water column and are in good agreement with previous studies (Palmer et al., 2008, 2015). In addition, we provide evidence of the sensitivity of the heat budget to various assumptions, such as thermocline limits, mixing efficiency and ε , which may measurably impact the outcome and should be considered.

5.2. Bulk Richardson Number and the Influence of Shear in Scalar Transport

To assess the role of shear in overcoming stratification to produce the observed dissipation rates and turbulent diffusivities, the bulk Richardson number (Ri_b) is defined for the thermocline region throughout C14 as

$$Ri_b \equiv \frac{g\Delta\rho h}{\rho_o(\Delta u)^2}, \quad (8)$$

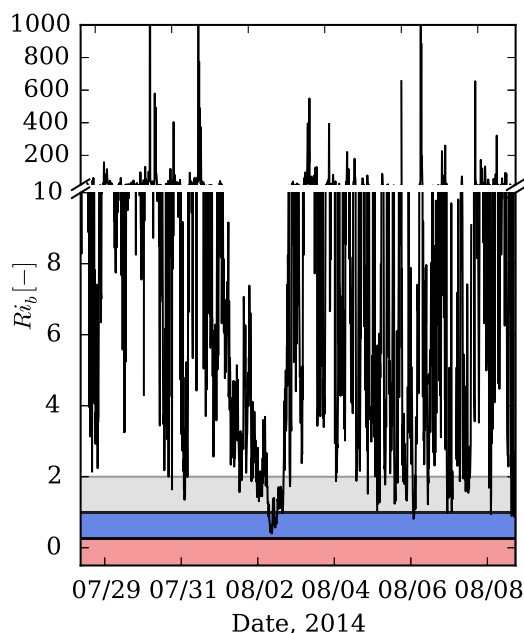


Figure 10. Bulk Richardson number during the C14 campaign. The gray shaded area underlines $1 \leq Ri_b \leq 2$ and the blue shaded area displays $0.25 \leq Ri_b \leq 1$. The red shaded area marks the $Ri_b \leq 0.25$ threshold, which is a necessary condition for turbulence to overcome stratification.

where Δu and $\Delta\rho$ represent the change in current velocity and the change in density between the top and the bottom of the thermocline. Velocities in the upper and lower layers are calculated using the ADCP data by averaging within bins located between 1 and 5 m above and below the top and bottom of the thermocline, respectively. These bins were found to be representative of across-thermocline shears, and do not include significant effects of the deviation of the current within the bottom boundary layer. Ri_b describes the stability of the thermocline in bulk, in which one estimate is obtained every 10 min.

If the thermocline and the shear layer have the same thickness and are centered with respect to each other, then $Ri_b < 1/4$ is a necessary condition for instability in stratified shear layers to develop (Hazel, 1972; Smyth et al., 2007). The resulting instabilities would be of the Kelvin-Helmholtz type causing an overturning of the density interface into the characteristic billow structure. In C14, the thermocline was dominated by stable stratification and weak shear. Figure 10 shows Ri_b for C14, which stayed well above the critical value $1/4$ during nearly the entire studied period. Of the estimated Ri_b values, 2% were less than or equal to 1 and 11% were less than or equal to 2. In periods where shear and stratification are roughly the same order of magnitude ($0.25 \leq Ri_b < 2$), the thermocline is often thought to be marginally stable and shear instabilities are potentially able to drive

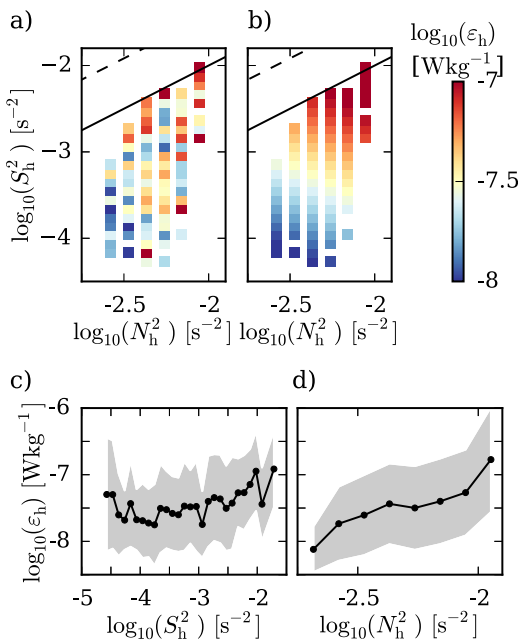


Figure 11. (a) Calculated and (b) parameterized dissipation of turbulent kinetic energy as a function of bulk thermocline stratification and shear. The black solid and dashed lines represent $Ri_b = 1$ and $Ri_b = 0.25$, respectively. Relationship between ϵ_h and (c) bulk thermocline shear squared and (d) buoyancy frequency squared. The gray shadows in Figures 11c and 11d represent 1 standard deviation from the mean.

our calculations are based on bulk values, ϵ is averaged across the thermocline and sorted in bins of bulk shear squared $S^2 \sim S_h^2 = \Delta U^2/h^2$ and bulk buoyancy frequency squared $N^2 \sim N_h^2 = g\Delta\rho/\rho_0 h$. Further, we compare the parameterization of MacKinnon and Gregg (2003), $\epsilon_{MG} = \epsilon_0(N/N_0)(S/S_0)$, with $S_0 = N_0 = 3$ cph and $\epsilon_0 = 5.5 \times 10^{-10} \text{ W kg}^{-1}$, to our observations. Here ϵ_0 was chosen to match the average of the parameterization (Figure 11b) with the observed mean value. Our results do not show a conclusive agreement with the parameterization (Figures 11a and 11b). Figure 11a depicts the mean dissipation values for each bin of bulk shear and stratification $\epsilon_h(N_h^2, S_h^2)$, which does not present a clear dependency on the bulk Richardson number. This seems reasonable considering that Ri_b remained stable throughout the campaign, while turbulence within the thermocline varied over several orders of magnitude. However, a tendency for low bulk Richardson numbers ($Ri_b \sim 1$) to be related to higher ϵ_h was found (Figure 11a).

A positive dependency is found between ϵ_h and N_h^2 and between ϵ_h and S_h^2 across the thermocline, with higher dissipation levels in strongly stratified and sheared areas (Figures 11c and 11d). Finally, if shear instabilities are responsible for triggering thermocline mixing, these results show that relatively small-scale sheared regions (<1 m) must be resolved in order to assess thermocline stability.

5.3. Alterations in Turbulence by Offshore Wind Farms

The technological development of offshore wind turbines has led to the planning and construction of offshore wind farms in areas of the North Sea that can exhibit stratification during the summer months. The installation of wind turbines in a region strongly influenced by tidal currents generate a turbulent wake. Assuming that the North Sea would be entirely covered by equally spaced (700–800 m) wind turbines, Carpenter et al. (2016) parameterized and tabulated turbulent production values for the German Bight sector of the North Sea based on standard bulk drag models. Depending on expected variations in the drag coefficient and on the foundation structure geometries, the average power production by turbine foundations that could be fed in to turbulence was estimated to be $\mathcal{P} = 4.6 \times 10^{-8} - 2.5 \times 10^{-7} \text{ W kg}^{-1}$ (Carpenter et al., 2016). These values should be considered as order of magnitude estimates and are assumed to be constant with depth.

turbulent mixing (Rippeth, 2005; Rippeth et al., 2005). This demonstrates, however, that the thermocline was stable to Kelvin-Helmholtz instabilities according to linear stability analysis, which is unsurprising given the absence of large-scale overturns of the thermocline. van Haren et al. (1999), Rippeth (2005), and Palmer et al. (2008) have hypothesized that the thermocline in European shelf seas can often be classified as marginally stable. This is based on the calculation of the gradient Richardson number, $Ri_g(z) = N^2/S^2$, where $S(z)$ denotes a measured vertical profile of shear, and instability becomes possible when $Ri_g(z) < 1/4$ somewhere in the water column. While Ri_g might be able to capture localized instabilities in the water column invisible to the bulk value, Ri_b , its calculation requires high-frequency (± 1 Hz) ADCP measurements, which are not available for our data set. Moreover, high-frequency ADCP measurements are necessary to meaningfully filter out the noise generated by the instrument itself without artificially thickening the shear layer and therefore decreasing Ri_g . In our analysis, subcritical values of the bulk Richardson number ($Ri_b < 1/4$) were not observed, indicating that the thermocline is stable to a large-scale overturn triggered by Kelvin-Helmholtz instability (Figure 10). However, the possibility remains that localized instabilities of shorter time scales are present on the edges of, or within, the thermocline.

Similar to other studies (van der Lee & Umlauf, 2011; Cyr et al., 2015; Palmer et al., 2008), we follow the procedure described in MacKinnon and Gregg (2003) to evaluate the relationship between shear, stratification, and the dissipation of turbulent kinetic energy. Since

The strength of dissipation of turbulent kinetic energy generated by turbine foundations, ε_{OWF} , can be obtained through the approximate conservation equation of the turbulent kinetic energy ($\mathcal{P} + \mathcal{B} - \varepsilon = 0$), where $\mathcal{B} = -\Gamma\varepsilon$ is the buoyancy flux. For simplicity, we set $\Gamma = 0.2$, and obtain the relation $\varepsilon_{OWF} \approx 0.8\mathcal{P}$. This simple equation suggests that the possible strength of the dissipation of turbulent kinetic energy generated by wind turbine foundations would be as high as 3.7×10^{-8} – 2.0×10^{-7} W kg^{-1} (Figure 3a).

Figure 3 shows that, on average, the turbulence generated by OWF foundations is expected to be in the same order of magnitude or weaker than bottom boundary layer turbulence, as already discussed by Carpenter et al. (2016). However, the addition of ε_{OWF} to the turbulent kinetic energy being dissipated in a natural stratified environment could enhance thermocline mixing significantly, as ε_{OWF} is estimated to be comparable to mean ε levels found in the thermocline. An increase in dissipation to this extent could locally drive the seasonal thermocline from a dominantly quiescent state to a highly turbulent state, enhancing mixing within stratification in the vicinity of the wind turbines. The response of the thermocline to anthropogenically induced enhanced levels of turbulent kinetic energy is however beyond the scope of this study and will be a topic of further study.

6. Conclusion

The present paper reports on extensive data sets for shallow shelf sea turbulence, allowing for the analysis of turbulence under stratified to well-mixed conditions over dozens of tidal cycles. We provided a direct comparison of the measured and estimated physical parameters between both regimes, enabling a better understanding of the processes governing scalar transport under stratified conditions. In recent years, the development of autonomous measurement platforms facilitates the execution of high-quality and -resolution experiments with a longer duration. The present study described observations from two different campaigns using underwater gliders equipped with microstructure sensors, which enabled the estimation of the dissipation of turbulent kinetic energy, turbulent diffusivity and turbulent activity index, in addition to the commonly measured CTD parameters. A bottom-mounted acoustic Doppler current profiler allowed the calculation of the bulk Richardson number, which was compared against turbulence levels.

We provide evidence of the intermittency of turbulence (Figures 5b, 7b, and 9), which can be triggered by various processes that occur sporadically and can be captured through long-term measurements with more confidence. For example, approximately 50% of the increase in bottom mixed layer temperature during the spiral missions was caused by four major events, whereas slow, background heat transfer dominated the fluxes otherwise. We therefore stress the importance of long-term measurements to adequately assess the dissipation of turbulent kinetic energy and related parameters (e.g., turbulent activity index and turbulent diffusivity) in the water column, and suggest glider-based platforms as a step forward.

While diffusion at molecular levels is abundantly present in the thermocline, turbulent mixing also takes place and contributes to vertical heat transport. Our results suggest that, on average, vertical mixing is the main mechanism driving scalar flux through the thermocline. A positive trend between bulk dissipation of turbulent kinetic energy, shear and stratification was found. Further enhanced levels of dissipation, turbulent activity index and turbulent diffusivity, which were continuously observed within the thermocline, might have been created by short-lived instabilities that are not resolved by the bulk Richardson number and by the ADCP. Future work could therefore focus on two different branches: (1) reducing the uncertainties linked with the estimation of ε , e.g., the verification of glider velocity; and (2) focusing on the study of small-scale shear (<1 m) to improve the understanding of turbulence generation across stably stratified thermoclines and to improve large-scale model parameterizations. As for shallow shelf seas strongly influenced by tidal motion, the impact of the additional turbulence generated by offshore wind farms should be further investigated, as the additional forcing being supplied to the water column and, more specifically, to the thermocline by turbine foundations could locally drive turbulence to levels significantly above those observed in a natural environment. This enhanced mixing could lead to higher scalar fluxes across stratification, possibly affecting its stability and leading to the erosion of the thermocline in

the vicinity of the turbine foundations, which could have further reaching implications on biological productivity.

Appendix A: Definition of the Turbulent Velocity Scale

A characteristic velocity of the turbulent flow is defined through dimensional analysis:

$$u_t \equiv (\varepsilon l_t)^{1/3}, \tag{A1}$$

where l_t is the turbulent length scale. The turbulent velocity scale, u_t , should be significantly lower than U for Taylor's hypothesis to hold (Fer et al., 2014). In turbulence regimes controlled by stratification, defined here as $N^2 > 10^{-5} \text{ s}^{-2}$, the Ozmidov length scale $L_O = (\varepsilon/N^3)^{1/2}$ characterizes the maximum possible length of a turbulent eddy, whereby $N^2 = (g/\rho_o)d\rho/dz$ represents the buoyancy frequency squared (e.g., Smyth et al., 2001). Additionally, to determine l_t for weakly stratified to well-mixed regimes, the Corrsin scale $L_C = (\varepsilon/S^3)^{1/2}$ is calculated, in which S represents a typical vertical profile of shear in the measurement region. The Corrsin scale determines the maximum length scale of an eddy in regimes dominated by shear (Corrsin, 1958; Smyth & Moum, 2000). Boundary effects in the water column also limit the size of turbulent eddies and are accounted for by estimating a third, geometric, length scale $L_G = \kappa z(1 - z/H_{\text{tot}})$ (Simpson & Sharples, 2012). In this equation, z is the height above bottom, H_{tot} is the water depth and $\kappa = 0.41$ is the von Kármán constant. The maximum turbulent length scale used to test for Taylor's hypothesis is ultimately estimated by taking $l_t = \min(L_O, L_G)$ for regions of the water column dominated by stratification and $l_t = \min(L_C, L_G)$ for weakly stratified to well-mixed areas:

$$l_t = \begin{cases} \min(L_O, L_G), & \text{if } N^2 > 10^{-5} \text{ s}^{-2} \\ \min(L_C, L_G), & \text{if } N^2 \leq 10^{-5} \text{ s}^{-2} \end{cases} \tag{A2}$$

Acknowledgments

The authors would like to thank the Helmholtz Foundation, which provided funding through the Polar Regions and Coasts in the Changing Earth System II program (PACES II). We also gratefully acknowledge the support of R. Kopetzky, M. Heineke, B. Peters, J. Horstmann, the captain and the crew of the research vessel (RV) *Ludwig Prandtl* and the *RV Heincke* in the collection of the glider data. The *RV Heincke* ship time was provided through the grant AWI_HE445_00. We thank the Bundesamt fuer Seeschiffahrt und Hydrographie (BSH) for the deployment and recovery of the ADCP in 2014. We would also like to thank both reviewers for their insightful comments on the paper. The glider data used are listed in the COSYNA repository at <http://codm.hzg.de/codm/>. The processed shear microstructure and the ADCP data are made available in the supporting information. Raw microstructure and ADCP data are available upon request.

References

- Baker, M. A., & Gibson, C. H. (1987). Sampling turbulence in the stratified ocean: Statistical consequences of strong intermittency. *Journal of Physical Oceanography*, 17(10), 1817–1836. [https://doi.org/10.1175/1520-0485\(1987\)017<1817:STITSO>2.0.CO;2](https://doi.org/10.1175/1520-0485(1987)017<1817:STITSO>2.0.CO;2)
- Bluteau, C. E., Jones, N. L., & Ivey, G. N. (2016). Estimating turbulent dissipation from microstructure shear measurements using maximum likelihood spectral fitting over the inertial and viscous subranges. *Journal of Atmospheric and Oceanic Technology*, 33(4), 713–722. <https://doi.org/10.1175/JTECH-D-15-0218.1>
- Bouffard, D., & Boegman, L. (2013). A diapycnal diffusivity model for stratified environmental flows. *Dynamics of Atmospheres and Oceans*, 61–62(June), 14–34. <https://doi.org/10.1016/j.dynatmoce.2013.02.002>
- Burchard, H., & Rippeth, T. P. (2009). Generation of bulk shear spikes in shallow stratified tidal seas. *Journal of Physical Oceanography*, 39(4), 969–985. <https://doi.org/10.1175/2008JPO4074.1>
- Carpenter, J. R., Merkelbach, L., Callies, U., Clark, S., Gaslikova, L., & Baschek, B. (2016). Potential impacts of offshore wind farms on North Sea stratification. *PLoS ONE*, 11(8), e0160830. <https://doi.org/10.1371/journal.pone.0160830>
- Corrsin, S. (1958). *Local isotropy in turbulent shear flow* (Res. Memo. RMS8B11). Washington, DC: National Advisory Committee for Aeronautics
- Cyr, F., Daniel, B., & Galbraith, P. S. (2015). Behavior and mixing of a cold intermediate layer near a sloping boundary. *Ocean Dynamics*, 65(3), 357–374. <https://doi.org/10.1007/s10236-014-0799-1>
- Fer, I., Peterson, A. K., & Ullgren, J. E. (2014). Microstructure measurements from an underwater glider in the turbulent Faroe Bank Channel overflow. *Journal of Atmospheric and Oceanic Technology*, 31(5), 1128–1150. <https://doi.org/10.1175/JTECH-D-13-00221.1>
- Franks, P. J. S. (2015). Has Sverdrup's critical depth hypothesis been tested? Mixed layers vs. turbulent layers. *ICES Journal of Marine Science*, 72(6), 1897–1907. <https://doi.org/10.1093/icesjms/fsu175>
- Garau, B., Ruiz, S., Zhang, W. G., Pascual, A., Heslop, E., Kerfoot, J., & Tintoré, J. (2011). Thermal lag correction on slocum CTD glider data. *Journal of Atmospheric and Oceanic Technology*, 28(9), 1065–1071. <https://doi.org/10.1175/JTECH-D-10-05030.1>
- Goodman, L., Levine, E. R., & Lueck, R. G. (2006). On measuring the terms of the turbulent kinetic energy budget from an AUV. *Journal of Atmospheric and Oceanic Technology*, 23(7), 977–990. <https://doi.org/10.1175/JTECH1889.1>
- Gregg, M. C., Alford, M. H., Kontoyiannis, H., Zervakis, V., & Winkel, D. (2012). Mixing over the steep side of the Cycladic Plateau in the Aegean Sea. *Journal of Marine Systems*, 89, 30–47. <https://doi.org/10.1016/j.jmarsys.2011.07.009>
- Hazel, P. (1972). Numerical studies of the stability of inviscid stratified shear flows. *Journal of Fluid Mechanics*, 51(1), 39–61. <https://doi.org/10.1017/S0022112072001065>
- Hebert, D. A., & de Bruyn Kops, S. M. (2006). Predicting turbulence in flows with strong stable stratification. *Physics of Fluids*, 18(6), 1–10. <https://doi.org/10.1063/1.2204987>
- Ho, A., Mbistrova, A., & Corbetta, G. (2016). *The European offshore wind industry: Key trends and statistics 2015* (Tech. rep.). Brussels, Belgium: The European Wind Energy Association.
- Holligan, P., Williams, P., Purdie, D., & Harris, R. (1984). Photosynthesis, respiration and nitrogen supply of plankton populations in stratified, frontal and tidally mixed shelf waters. *Marine Ecology Progress Series*, 17, 201–213. <https://doi.org/10.3354/meps017201>
- Huisman, J., Sharples, J., Stroom, J. M., Visser, P. M., Kardinaal, W. E. A., Verspagen, J. M. H., & Sommeijer, B. (2004). Changes in turbulent mixing shift competition for light between phytoplankton species. *Ecology*, 85(11), 2960–2970. <https://doi.org/10.1890/03-0763>
- Huthnance, J. (1991). Physical oceanography of the North Sea. *Ocean and Shoreline Management*, 16(3–4), 199–231. [https://doi.org/10.1016/0951-8312\(91\)90005-M](https://doi.org/10.1016/0951-8312(91)90005-M)

- Itsweire, E. C., Helland, K. N., & Van Atta, C. W. (1986). The evolution of grid-generated turbulence in a stably stratified fluid. *Journal of Fluid Mechanics*, 162(1986), 299–338. <https://doi.org/10.1017/S0022112086002069>
- Ivey, G., Winters, K., & Koseff, J. (2008). Density stratification, turbulence, but how much mixing? *Annual Review of Fluid Mechanics*, 40(1), 169–184. <https://doi.org/10.1146/annurev.fluid.39.050905.110314>
- Lauria, M. L., Purdie, D. A., & Sharples, J. (1999). Contrasting phytoplankton distributions controlled by tidal turbulence in an estuary. *Journal of Marine Systems*, 21(1–4), 189–197. [https://doi.org/10.1016/S0924-7963\(99\)00013-5](https://doi.org/10.1016/S0924-7963(99)00013-5)
- Ledwell, J. R., Duda, T. F., Sundermeyer, M. A., & Seim, H. E. (2004). Mixing in a coastal environment: 1. A view from dye dispersion. *Journal of Geophysical Research*, 109, C10013. <https://doi.org/10.1029/2003JC002194>
- Lueck, R. (2013). *Calculating the rate of dissipation of turbulent kinetic energy* (Tech. Note TN-028, 18 pp.). Victoria, BC: Rockland Scientific International Inc. Retrieved from <http://rocklandscientific.com/?wpdmdl=1034>
- Lueck, R. G., & Picklo, J. J. (1990). Thermal inertia of conductivity cells: Observations with a sea-bird cell. *Journal of Atmospheric and Oceanic Technology* 7, 756–768. [https://doi.org/10.1175/1520-0426\(1990\)007<0756:TIOCCO>2.0.CO;2](https://doi.org/10.1175/1520-0426(1990)007<0756:TIOCCO>2.0.CO;2)
- Lueck, R. G., Wolk, F., & Yamazaki, H. (2002). Oceanic velocity microstructure measurements in the 20th century. *Journal of Oceanography*, 58, 153–174.
- Mackinnon, J. A., & Gregg, M. C. (2003). Mixing on the late-summer New England shelf-solibores, shear, and stratification. *Journal of Physical Oceanography*, 33(7), 1476–1492. [https://doi.org/10.1175/1520-0485\(2003\)033<1476:MOTLNE>2.0.CO;2](https://doi.org/10.1175/1520-0485(2003)033<1476:MOTLNE>2.0.CO;2)
- Merkelbach, L., Smeed, D., & Griffiths, G. (2010). Vertical water velocities from underwater gliders. *Journal of Atmospheric and Oceanic Technology*, 27(3), 547–563. <https://doi.org/10.1175/2009JTECHO710.1>
- Morison, J., Andersen, R., Larson, N., D'asaro, E., & Boyd, T. (1994). The correction for thermal-lag effects in sea-bird CTD data. *Journal of Atmospheric and Oceanic Technology*, 11(4), 1151–1164. [https://doi.org/10.1175/1520-0426\(1994\)011<1151:TCFTLE>2.0.CO;2](https://doi.org/10.1175/1520-0426(1994)011<1151:TCFTLE>2.0.CO;2)
- Muller-Karger, F. E., Varela, R., Thunell, R., Luerssen, R., Hu, C., & Walsh, J. J. (2005). The importance of continental margins in the global carbon cycle. *Geophysical Research Letters*, 32, L01602. <https://doi.org/10.1029/2004GL021346>
- Nasmyth, P. W. (1970). *Ocean turbulence* (PhD thesis). Vancouver, BC: University of British Columbia.
- Osborn, T. R. (1980). Estimates of the local rate of vertical diffusion from dissipation measurements. *Journal of Physical Oceanography*, 10, 83–89. [https://doi.org/10.1175/1520-0485\(1980\)010<0083:EOTLRO>2.0.CO;2](https://doi.org/10.1175/1520-0485(1980)010<0083:EOTLRO>2.0.CO;2)
- Palmer, M. R., Rippeth, T. P., & Simpson, J. H. (2008). An investigation of internal mixing in a seasonally stratified shelf sea. *Journal of Geophysical Research*, 113, C12005. <https://doi.org/10.1029/2007JC004531>
- Palmer, M. R., Stephenson, G. R., Inall, M. E., Balfour, C., Düsterhus, A., & Green, J. A. M. (2015). Turbulence and mixing by internal waves in the Celtic Sea determined from ocean glider microstructure measurements. *Journal of Marine Systems*, 144, 57–69. <https://doi.org/10.1016/j.jmarsys.2014.11.005>
- Pingree, R. D., & Griffiths, D. K. (1978). Tidal fronts on the shelf seas around the British Isles. *Journal of Geophysical Research*, 83(C9), 4615–4622. <https://doi.org/10.1029/JC083iC09p04615>
- Richardson, K., Nielsen, T., Pedersen, F., Heilman, J., & Løkkegaard, B. and Kaas, H. (1998). Spatial heterogeneity in the structure of the planktonic food web in the North Sea. *Marine Ecology Progress Series*, 168, 197–211. <https://doi.org/10.3354/meps168197>
- Rippeth, T. P. (2005). Mixing in seasonally stratified shelf seas: A shifting paradigm. *Philosophical Transactions. Series A, Mathematical, Physical, and Engineering Sciences*, 363(1837), 2837–2854. <https://doi.org/10.1098/rsta.2005.1662>
- Rippeth, T. P., Palmer, M. R., Simpson, J. H., Fisher, N. R., & Sharples, J. (2005). Thermocline mixing in summer stratified continental shelf seas. *Geophysical Research Letters*, 32, L05602. <https://doi.org/10.1029/2004GL022104>
- Ross, O. N., & Sharples, J. (2007). Phytoplankton motility and the competition for nutrients in the thermocline. *Marine Ecology Progress Series*, 347, 21–38. <https://doi.org/10.3354/meps06999>
- Shih, L. H., Koseff, J. R., Ivey, G. N., & Ferziger, J. H. (2005). Parameterization of turbulent fluxes and scales using homogeneous sheared stably stratified turbulence simulations. *Journal of Fluid Mechanics*, 525(August), 193–214. <https://doi.org/10.1017/S0022112004002587>
- Simpson, J. H., Brown, J., Matthews, J., & Allen, G. (1990). Tidal straining, density currents, and stirring in the control of estuarine stratification. *Estuaries*, 13(2), 125–132. <https://doi.org/10.2307/1351581>
- Simpson, J. H., Crawford, W. R., Rippeth, T. P., Campbell, A. R., & Cheok, J. V. S. (1996). The Vertical structure of turbulent dissipation in shelf seas. *Journal of Physical Oceanography*, 26(8), 1579–1590. [https://doi.org/10.1175/1520-0485\(1996\)026<1579:TVSOTD>2.0.CO;2](https://doi.org/10.1175/1520-0485(1996)026<1579:TVSOTD>2.0.CO;2)
- Simpson, J. H., & Sharples, J. (2012). *Introduction to the physical and biological oceanography of shelf seas* (424. pp.). Cambridge, UK: Cambridge University Press.
- Smyth, W. D., & Moum, J. N. (2000). Anisotropy of turbulence in stably stratified mixing layers. *Physics of Fluids*, 12(6), 1327–1362. <https://doi.org/10.1063/1.870385>
- Smyth, W. D., Carpenter, J. R., & Lawrence, G. A. (2007). Mixing in symmetric Holmboe waves. *Journal of Physical Oceanography*, 37(6), 1566–1583. <https://doi.org/10.1175/JPO3037.1>
- Smyth, W. D., Moum, J. N., & Caldwell, D. R. (2001). The efficiency of mixing in turbulent patches: Inferences from direct simulations and microstructure observations. *Journal of Physical Oceanography*, 31(8), 1969–1992. [https://doi.org/10.1175/1520-0485\(2001\)031<1969:TEOMIT>2.0.CO;2](https://doi.org/10.1175/1520-0485(2001)031<1969:TEOMIT>2.0.CO;2)
- Stillinger, D. C., Helland, K. N., & Van Atta, C. W. (1983). Experiments on the transition of homogeneous turbulence to internal waves in a stratified fluid. *Journal of Fluid Mechanics*, 131, 91–122. <https://doi.org/10.1017/S0022112083001251>
- Thorpe, S. (2007). *An introduction to ocean turbulence* (264 pp.). Cambridge, UK: Cambridge University Press.
- van der Lee, E. M., & Umlauf, L. (2011). Internal wave mixing in the Baltic Sea: Near-inertial waves in the absence of tides. *Journal of Geophysical Research*, 116, C10016. <https://doi.org/10.1029/2011JC007072>
- van Haren, H., Maas, L. R. M., Zimmerman, J. T. F., Ridderinkhof, H., & Malschaert, H. (1999). Strong inertial currents and marginale internal wave stability in the central North Sea. *Geophysical Research Letters*, 26(19), 2993–2996.
- van Leeuwen, S., Tett, P., Mills, D., & van Der Molen, J. (2015). Stratified and nonstratified areas in the North Sea: Long-term variability and biological and policy implications. *Journal of Geophysical Research: Oceans*, 120, 4670–4686. <https://doi.org/10.1002/2014JC010485>
- Walter, R. K., Squibb, M. E., Woodson, C. B., Koseff, J. R., & Monismith, S. G. (2014). Stratified turbulence in the nearshore coastal ocean: Dynamics and evolution in the presence of internal bores. *Journal of Geophysical Research: Oceans*, 119, 8709–8730. <https://doi.org/10.1002/2014JC010396>
- Wolk, F., & Lueck, R. G. (2009). Turbulence measurements from a glider. Paper presented at 13th Workshop on Physical Processes in Natural Waters, Palermo, Italy.
- Wolk, F., Yamazaki, H., Seuront, L., & Lueck, R. G. (2002). A new free-fall profiler for measuring biophysical microstructure. *Journal of Atmospheric and Oceanic Technology*, 19(5), 780–793. [https://doi.org/10.1175/1520-0426\(2002\)019<0780:ANFFPF>2.0.CO;2](https://doi.org/10.1175/1520-0426(2002)019<0780:ANFFPF>2.0.CO;2)